

Contents lists available at ScienceDirect

# Urban Climate

journal homepage: www.elsevier.com/locate/uclim



# Development and testing of a fully-coupled subsurface-land surface-atmosphere hydrometeorological model: High-resolution application in urban terrains

Mahdad Talebpour a,\*, Claire Welty a, Elie Bou-Zeid b

### ARTICLE INFO

# Keywords: Urban hydrometeorology Urban groundwater Coupled atmosphere-land surface-subsurface modeling Large-eddy simulation

### ABSTRACT

To improve simulation of atmospheric-hydrological processes with shallow groundwater in urban areas, a new fully-coupled model was developed. The Weather Research and Forecasting (WRF) atmospheric model in the large-eddy-simulation (LES) mode, the Princeton Urban Canopy Model (PUCM), and the subsurface hydrological model ParFlow (PF) were linked (WRF-PUCM-PF). To evaluate the impact of coupling, model intercomparison was performed by application to a small watershed in suburban Baltimore, Maryland, USA, for scenarios of both homogeneous and heterogeneous geologic properties, using WRF-PUCM with and without the ParFlow component. Homogeneous scenarios isolated the impact of including terrestrial hydrological processes through ParFlow. In response to rain events, the homogeneous WRF-PUCM model output gained and retained a 40% greater amount of soil moisture (area-averaged) compared to the homogeneous WRF-PUCM-PF case. In heterogeneous scenarios, the WRF-PUCM model generated a 10fold greater area-averaged soil moisture increase over the simulation period compared to the WRF-PUCM-PF case. The WRF-PUCM-PF model output, influenced by lateral hydrology and impervious surfaces, generated lower latent heat flux, resulting in half of the domain having higher land surface temperatures (2-10 °C), compared to the WRF-PUCM model. Overall, the WRF-PUCM-PF model provides a new tool to simulate urban physics and resolve finer urban microclimatic heterogeneity.

# 1. Introduction

Studies have shown how urban growth and anthropogenic activities contribute to phenomena such as climate change and urban heat island (UHI) effects (Block et al., 2004; Seto and Shepherd, 2009; Liu et al., 2012; Ren, 2015; Lopez and Maxwell, 2016). In turn, these atmospheric-hydrological phenomena, and their interconnectivity, can impact the health of populations and ecosystems. Untangling the complexity of coupled urban atmospheric-hydrological processes is essential for improving sustainable and resilient development.

One of the main challenges in modeling physical processes in urban regions is developing accurate parameterization schemes for

E-mail address: mahdad1@umbc.edu (M. Talebpour).

<sup>&</sup>lt;sup>a</sup> Department of Chemical, Biochemical, and Environmental Engineering and Center for Urban Environmental Research and Education, University of Maryland Baltimore County, Baltimore, MD, United States of America

b Department of Civil and Environmental Engineering, Princeton University, Princeton, NJ, United States of America

<sup>\*</sup> Corresponding author at: 1000 Hilltop Circle, Technology Research Center, RM:102, University of Maryland Baltimore County, Baltimore, MD 21250, United States of America.

use in physically-based geophysical models. Urban regions have distinct characteristics that affect hydrological-atmospheric processes at the land surface, in the upper subsurface, and in the lower atmosphere (Fig. 1). As these effects can strongly alter energy and water cycle in cities, it is essential to represent these elements or their effects through appropriate parameterization schemes in atmospheric-hydrological models. In the past, efforts have been made to improve representation of urban distinct features in atmospheric-hydrological models (Wang et al., 2013; Li and Bou-Zeid, 2014; Vahmani and Hogue, 2014; Bhaskar et al., 2015; Ryu et al., 2016a; Varlas et al., 2018; Mauree et al., 2018; Meili et al., 2020; Spyrou et al., 2020), compared to their counterparts used to model more undisturbed systems.

Wang et al. (2013) developed the Princeton Urban Canopy Model (PUCM) to improve physical representation of heterogeneous energy and water balances at the urban land surface. PUCM enhances representation of water and energy balances by adding schemes to simulate urban heterogeneous subfacets consisting of different materials (Li et al., 2014; Ramamurthy et al., 2014). Li and Bou-Zeid (2014) incorporated PUCM into the Weather Research and Forecasting model (WRF; Skamarock et al., 2008) and compared output to that of WRF with its original/default Urban Canopy Model (UCM). Validated against in-situ and remotely-sensed observations, WRF-PUCM showed the smallest bias (<1.5 °C) in urban surface temperature fields. Overall, land surface temperature (LST) and associated UHI intensity predictions were improved using PUCM. Implementation of subfacet heterogeneity of thermal parameterization enabled investigation of UHI mitigation strategies, such as white roofs. Several investigations have since used WRF-PUCM to evaluate urban atmospheric-hydrological processes. In a study of the influence of land-surface heterogeneities on heavy convective rainfall, Ryu et al. (2016b) found better performance using WRF-PUCM in reproducing the surface energy balance and the rainfall than the traditional slab model for the urban area. However, in all of these studies, the representation of the subsurface was simplified to vertical isolated soil columns with 4 layers, the representation adopted in the Noah land surface model (LSM).

Terrestrial hydrological processes, however, are more complex and can be strongly coupled to atmospheric dynamics. In areas with persistently or intermittently shallow groundwater, the atmospheric-hydrological coupling becomes a leading driver of hydrometeorology and influences the energy and water cycle at the land surface, in the upper subsurface, and in the lower atmosphere. Several

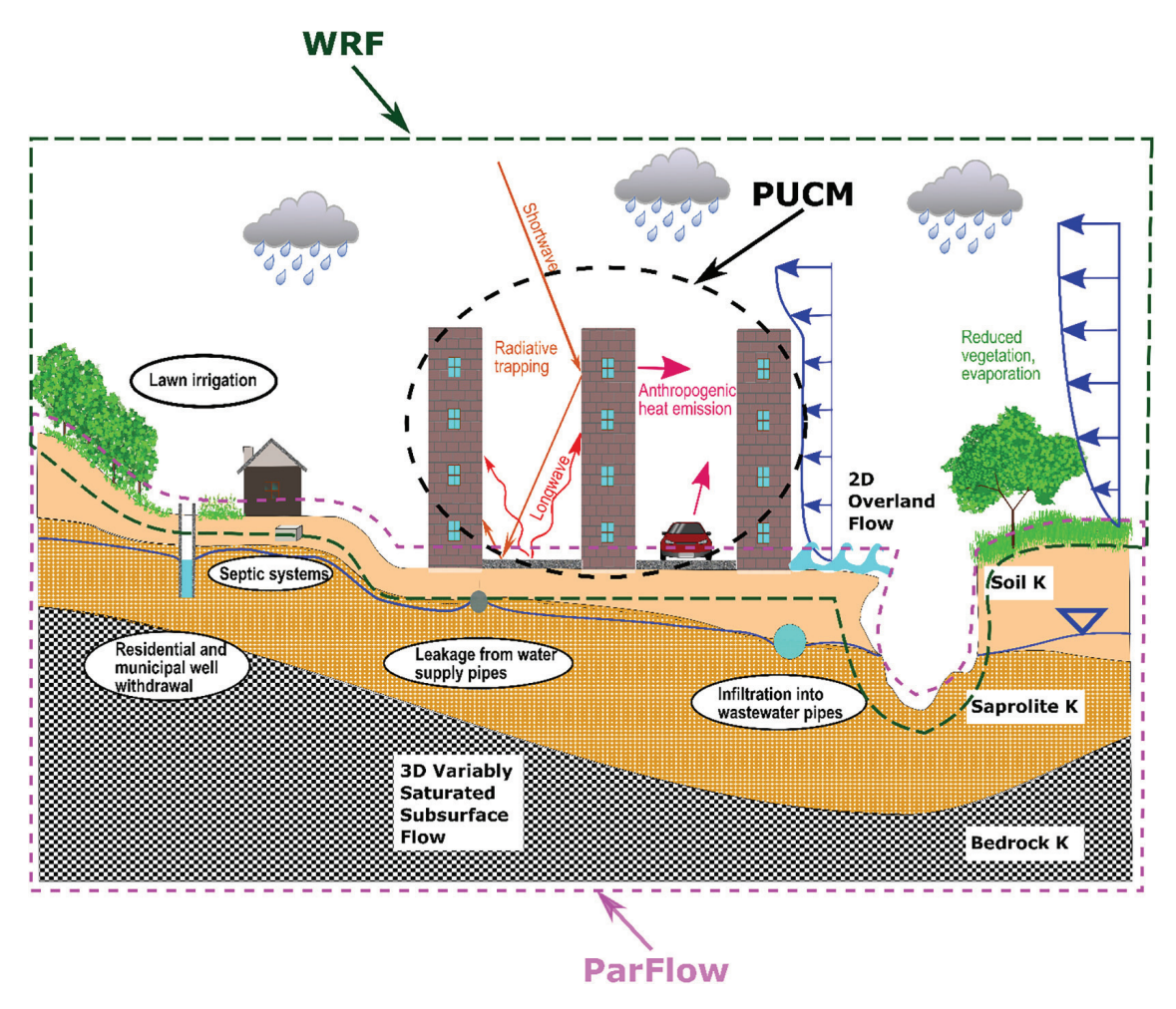


Fig. 1. Schematic diagram of distinct atmospheric-hydrological features and processes in urban areas. The pink, green, and black dashed lines encapsulate schematically the parts of subsurface, land surface, and atmosphere that are being modeled by ParFlow, WRF, and PUCM. Not all the fluxes in the figure are represented in the models. ParFlow and WRF exchange fluxes and are connected at the top soil layers in the subsurface (Maxwell et al., 2011). PUCM is used to calculate surface energy fluxes over the urban part of the land surface. (For interpretation of the references to colour in this figure legend, the reader is referred to the web version of this article.)

studies have incorporated physically realistic fully-coupled atmosphere-land surface-subsurface models to evaluate interconnectivity of terrestrial and atmospheric processes and their influences on the hydrometeorological processes (Maxwell et al., 2011; Shrestha et al., 2014; Senatore et al., 2015; Wagner et al., 2016; Fersch et al., 2020). Noah is the most widely used LSM model in WRF (Chen and Dudhia, 2001); it utilizes a diffusive form of the one-dimensional Richards equation with an assumption of a rigid and homogeneous vertical flow domain, in which cells are isolated horizontally from each other (Appendix A). Therefore, lateral hydrological fluxes are not captured in models utilizing Noah, including WRF-PUCM. This framework might be suitable when applied with coarse model resolutions (e.g. the typical WRF grid resolution used for weather forecasting is  $\sim$ 9 km  $\times$  9 km) where the lateral redistribution of water on the surface and in the subsurface between adjacent cells is much smaller than the vertical fluxes. However, this assumption breaks down as model resolution improves, leading Maxwell et al. (2011) to develop a fully-coupled atmospheric-hydrological model ParFlow-WRF (PF.WRF), using Noah as the connector to incorporate terrestrial hydrology (as represented by ParFlow) into WRF. They demonstrated how lateral overland and subsurface water flow components in PF.WRF distributed soil moisture in a more physically realistic manner compared to WRF-Noah.

The need to account for terrestrial hydrology is further accentuated in urban areas that bring about more complexity to coupled atmosphere-groundwater interactions influenced by different urban development patterns. Barnes et al. (2018), utilizing a land surface-subsurface model (ParFlow-CLM), demonstrated how groundwater could contribute to evapotranspiration annually during water-limited days in watersheds with shallow depth-to-groundwater. The authors also showed how water infiltrating into pervious areas and subsequently flowing under impervious areas was inhibited from evaporating as it became trapped under low-permeability surfaces. This behavior resulted in a highly variable contribution of subsurface storage to evapotranspiration and soil moisture across urban surfaces. These water fluxes will significantly modulate energy fluxes.

It is now well established that soil moisture distribution plays an essential role in modulating land surface energy and water fluxes. Discrepancies in the prediction of soil moisture evolution could therefore have significant implications for urban atmospheric predictions. Ramamurthy and Bou-Zeid (2017), using WRF-PUCM, showed that northeastern U.S. cities with higher population and population density (New York, New York, USA; Philadelphia, Pennsylvania, USA; Washington, District of Columbia, USA; and Baltimore, Maryland, USA), exhibit sharp gradients in surface soil moisture along the urban-suburban-rural transect, explaining their UHI patterns. In turn, the lack of soil moisture at local urban scales can lead to disproportionately higher sensible heat compared to rural areas and exacerbates UHI effects. Manoli et al. (2019) and Manoli et al. (2020) introduced a coarse-grained global scale model that demonstrated the strong links between precipitation, as a proxy for background hydroclimate and UHI intensity. They found that summertime differences between urban to rural surface temperatures (ΔT) increase nonlinearly with annual precipitation and are modulated by its seasonal cycle and that this was tied to urban-rural differences in evapotranspiration.

As described by Ramamurthy and Bou-Zeid (2014), modification of hygrothermal properties in urban areas makes hydrological modeling particularly challenging because spatial heterogeneity exists at fine scales, thus altering energy and water balances at fine scales, as well as flow and transport in the atmospheric boundary layer (ABL) (Bou-Zeid et al., 2020). Moreover, land surface topography is also highly altered at fine grid resolutions in urban areas. If the impacts of land surface heterogeneity are important to modeling goals, then fine-scale discretization of landscape features may also be warranted for modeling terrestrial hydrology. At scales finer than 1 km, mesoscale Reynolds-Averaged Navier-Stocks (RANS) methods encoded as PBL parameterization schemes in atmospheric models cannot be used, because approximations of RANS models made in resolving turbulent flows at mesoscales do not hold (Wyngaard, 2004; Nahian et al., 2020). The Large-Eddy Simulation (LES) approach is then more suitable, and it is capable of resolving large turbulent eddies transporting heat, mass, and momentum in the atmospheric boundary layer, while atmospheric dynamic structures smaller than the grid size are parameterized. Running LES studies is becoming more common, due to advances in computational resources, to study urban areas at fine atmospheric grid scales (i.e., < 100 m) (Park et al., 2015; García-Sánchez et al., 2018; Wiersema et al., 2020). Parameterizations for LES have been implemented in WRF. Although WRF-LES was first developed for ideal cases, Talbot et al. (2012) introduced a framework to apply WRF-LES to real domains. They used nesting capability in WRF to dynamically downscale boundary conditions over highly complex terrain, from mesoscale to microscale.

The focus of this study is to identify how modification of terrestrial hydrology affects urban simulation of hydrometeorological processes at fine scales. Fine-scale urban atmospheric-hydrological modeling has been conducted in the past, but only in an uncoupled mode and often at disparate resolutions. Fully-coupled atmospheric-hydrological modeling of urban areas at fine scales has not yet been conducted; this is a significant identified research gap. To address this research need, the objectives of this study are: (1) to couple WRF-PUCM and ParFlow (WRF-PUCM-PF); (2) to utilize WRF-PUCM-PF in LES mode and with a nesting framework to conduct simulations at high grid resolutions (90-m example here); and (3) to compare and contrast the spatial fields simulated by WRF-PUCM-PF with WRF-PUCM in test-case scenario simulations of the urban water and energy cycles. The goal here is to conduct a model intercomparison study, rather than model validation.

Section 2 describes each model component used in this study and delves into the details of coupling technique used to link WRF-PUCM and ParFlow, to build WRF-PUCM-PF. In part 2 of Section 2, the case scenario simulations designed to compare WRF-PUCM-PF performance against WRF-PUCM are described. The results and discussion pertaining to the case scenarios are explained in Section 3. Finally, Section 4 summarizes the findings of this study and provides the concluding remarks for this study.

### 2. Methods

# 2.1. Model descriptions

The methodology used in this work brings together three components for advancing hydrological-atmospheric modeling of urban

areas: (1) WRF-LES and nesting methods for field scenarios; (2) the PUCM implementation in WRF for modeling heterogeneous urban surfaces; and (3) ParFlow, a surface-subsurface terrestrial hydrology model. The result is a fully-coupled urban subsurface-land surface-atmosphere modeling approach.

### 2.1.1. WRF-LES

The Weather Research and Forecasting (WRF) model is an open-source model designed for both research and operational use (Skamarock et al., 2008). WRF solves mass, momentum, and energy balance equations, using traditional and terrain-following mass coordinates. WRF utilizes a variety of numerical and physical parameterization schemes to account for atmospheric and land surface physical processes including radiation, precipitation, and land-surface energy and water fluxes. As with other atmospheric models, PBL schemes were employed in WRF for mesoscale simulations, which is relevant for grid resolutions >1 km. At grid resolutions <1 km, including the urban-relevant grid resolution of 90 m chosen for this study, the LES approach can be used to resolve the dynamics of the atmosphere. The framework introduced by Talbot et al. (2012) was used to apply WRF-LES to the domain of study. The nesting capability in WRF dynamically downscales boundary conditions over highly complex terrain, from mesoscale to microscale. This approach provides LES simulations in the desired domain with appropriate boundary conditions.

# 2.1.2. WRF-PUCM

WRF-PUCM simulates urban canopy features such as radiative trapping due to building forms (Wang et al., 2011; Li and Bou-Zeid, 2013, 2014). PUCM assigns a heterogeneous subfacet in its single-layer resistance network of energy and water transport, whereas common UCM models do not account for such heterogeneity. When PUCM is used in WRF, an urban grid cell (which is defined based on land cover maps), is divided into two parts: an impervious part and a vegetated part. Noah and PUCM compute surface energy balances for vegetated and impervious fractions of model cells, respectively. The final fluxes and state variables of a grid cell are computed as weighted averages of these values based on the fractions of land use computed from land cover maps. All terrestrial hydrology processes are modeled through Noah. Noah implements a one-dimensional representation of subsurface hydrology (Appendix A).

### 2.1.3. ParFlow

ParFlow is an open-source, variably saturated subsurface flow model with an integrated overland flow component (Ashby and Falgout, 1996; Jones and Woodward, 2001; Maxwell, 2013; Kollet and Maxwell, 2006). ParFlow solves the Richards equation for three-dimensional, variably-saturated subsurface flow and the two-dimensional kinematic wave equation for surface flow, enabling simulation of integrated, spatially-distributed surface and subsurface flow (Appendix A).

Available to ParFlow users are computational tools for incorporation of 3D subsurface hydrogeological properties. ParFlow includes an option to assign subsurface layers with variable thicknesses, enabling a computationally efficient approach for integrating subsurface properties at large depths.

ParFlow has an option for coupling to the Common Land Model (CLM) LSM (Dai et al., 2003) to simulate land surface energy and water fluxes, using atmospheric forcing data (Maxwell and Miller, 2005; Kollet and Maxwell, 2008). In this study, CLM was used only for standalone ParFlow spin-up simulations (not coupled to WRF-PUCM) of the domain of interest; for the fully-coupled simulations, the LSM was switched to Noah inside WRF with direct coupling to ParFlow.

# 2.1.4. Coupled WRF-PUCM-PF in the LES mode

The approach developed by Maxwell et al. (2011) was utilized to couple ParFlow to WRF-PUCM. In WRF-PUCM-PF, the Noah LSM module residing within WRF is the component connecting the terrestrial hydrology (ParFlow) to the atmosphere (WRF). All terrestrial hydrology in Noah is replaced by ParFlow as a subroutine (Appendix A). The combination of improved parameterization of urban fluxes and balances in PUCM and ParFlow's capability to represent distinct urban hydrological features enhances the physical representation of urban areas in a fully-coupled manner. Moreover, LES schemes in WRF enable capturing dynamic interactions at high resolutions (e.g., 90 m in the test case used here) between the turbulence eddies and the highly heterogeneous urban land surface.

# 2.2. Test cases: numerical methods and computational setups

To test the performance of the fully-coupled model, WRF-PUCM-PF, and to compare its performance to WRF-PUCM, two series of simulations were run on a test domain: a homogenous subsurface setup; and a heterogeneous subsurface setup. This simulation design aimed to isolate any effects of subsurface heterogeneity on model output. These case scenarios were designed to demonstrate how different aspects of urban hydrologic representation could impact soil moisture distribution in a simulation.

# 2.2.1. Model input

This study used 1/9th arc-second USGS digital elevation models (DEMs) data (https://www.usgs.gov/core-science-systems/ngp/3dep), processed for both ParFlow and WRF. For land cover input, the USGS 30-m National Land Cover Data (NLCD) dataset was resampled for input in ParFlow-CLM stand-alone simulations and WRF-Noah in all other stand-alone and coupled simulations. North American Land Data Assimilation System (NLDAS2, https://ldas.gsfc.nasa.gov/nldas/NLDAS2forcing.php) hourly atmospheric forcing data, at 1/8th of a degree, were used for ParFlow-CLM stand-alone simulations to spin-up the subsurface component. For WRF simulations, NCEP North American Regional Reanalysis (NARR, https://www.ncdc.noaa.gov/data-access/model-data/model-datasets/north-american-regional-reanalysis-narr) 3-hourly atmospheric forcing data, at 32 km resolution, were used to drive the initial and boundary conditions at the largest simulation domains.

### 2.2.2. Computational setup

Computational experiments were carried out using data for a small watershed in suburban Baltimore, Maryland (Dead Run) as a test domain for the finest-grid resolution of interest. Fig. 2 shows the innermost domain extent (~117 km²), fraction of impervious surface area, and topography. The domain was chosen to be small enough to run numerous case scenarios in a computationally feasible timeframe while large enough to be characterized by spatially variable atmospheric and hydrological processes.

The number of horizontal cells chosen was 120 by 120 (14400) with a 90-m grid resolution, providing a domain extent in both north-south and east-west directions of 10.8 km. The number of vertical atmospheric layers specified was 108 to capture fine-scale processes near the land surface, following recommendations by Talbot et al. (2012) for WRF-LES studies. Twelve subsurface layers were used in ParFlow, for a total thickness up to 31 m following the subsurface setup by Barnes et al. (2018). The 12 layers were designed to capture subsurface heterogeneity in terms of soil, saprolite, highly weathered bedrock (transition zone), and fractured bedrock. For WRF-PUCM-PF, the top four layers' depth in ParFlow were identical to the top four layers in Noah to allow for flux exchanges between ParFlow and Noah. The dimensions of these layers are summarized in Table 1. The hydrogeological properties were different in homogeneous and heterogeneous case scenarios. The 12 subsurface layers in ParFlow served two purposes: (1) to mimic free drainage at the bottom of the fourth layer in the WRF-PUCM model; (2) to allow for implementation of 3D subsurface hydrogeological properties following the work done by Barnes et al. (2018), for the heterogeneous-case scenarios.

All the simulations pertain to a period of 112 h starting from July 18, 2008, at 20:00 Eastern Daylight Time (EDT, July 19, 2008, at 00:00 GMT) to July 23, 2008, at 12:00 EDT. This period was selected to compare the two model responses to a dry-down period at the beginning of the simulations followed by several rain events. The first four hours of the coupled simulation, starting from July 18, 2008, at 20:00 EDT to July 19, 2008, at 00:00 EDT, were used for spinning up the atmospheric dynamics and turbulence and were not used in the analyses.

## 2.2.3. ParFlow setup and spinup

ParFlow was run using options for terrain-following grid (TFG) and variable DZ (subsurface vertical grid resolution). The DEM processing method developed by Barnes et al. (2016) was used to generate required slope files. The time step used in ParFlow spin-up simulations was 1 h based on NLDAS hourly input forcing data. Boundary conditions at the four lateral boundaries and the bottom of the ParFlow subsurface domain were set to zero flux.

ParFlow spin-up was conducted to initialize identical soil moisture distributions in WRF-PUCM and WRF-PUCM-PF simulations. Recommendations described in Seck et al. (2015) were used. Atmospheric forcing data were processed for a year prior to the start of the analysis period, from July 1st, 2007 to June 30th, 2008. Spin-up was repeated for six and nine years for the homogeneous and heterogeneous geology setups, respectively until an equilibrium state was reached. In this study, subsurface storage change was used as the evaluation parameter for reaching equilibrium. For each time step, the computed total subsurface storage of the current year minus the previous year, divided by the current year was used. When this normalized change reached a value of less than 0.005, it was assumed that an equilibrium state was approximately achieved. ParFlow was run for an additional 18 days from July 1st, 2008 to July 18, 2008, to get to the start of the analysis period.

# 2.2.4. WRF-LES setup

WRF's nesting feature was employed to simulate multiple domains. A series of nested simulations were run, ranging from mesoscale to microscale, all centered on the smallest domain of study (Fig. 3), to downscale inflow boundary conditions to the desired domain (Fig. 2). Considering 90 m as the target innermost domain resolution, the five domains chosen had 12150-, 4050-, and 1350-m resolutions run in mesoscale RANS mode, followed by 270- and 90-m resolution domains run in LES mode (Fig. 3). The nested simulations

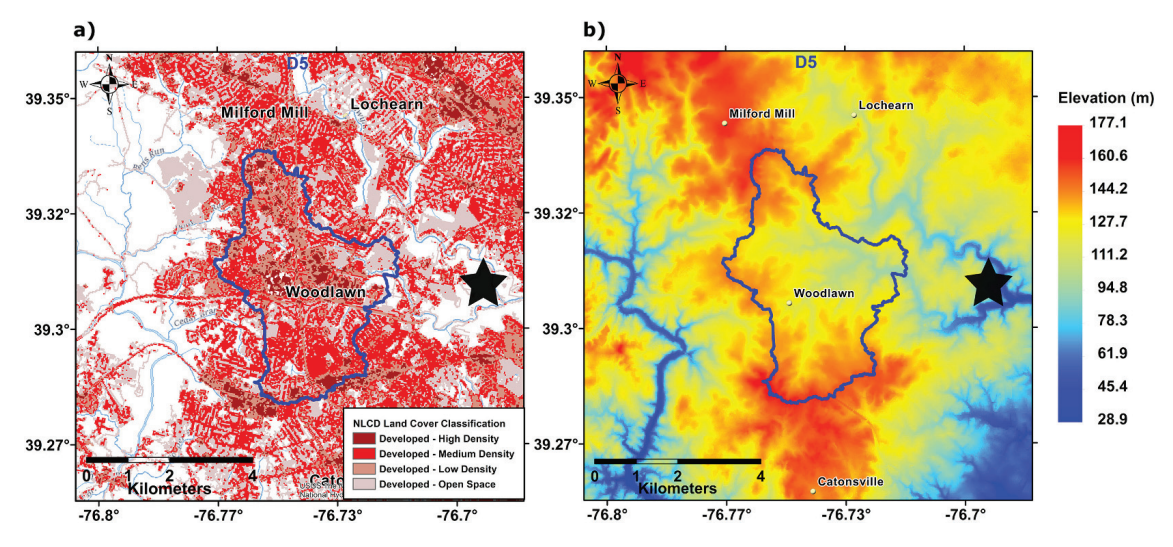


Fig. 2. The domain of study; a) innermost WRF-PUCM-PF domain (Fig. 3), encompassing Dead Run watershed. The black star shows the Leakin park area; b) elevation map for the domain.

Table 1
Subsurface dimensional and hydrogeologic properties of layers (based on Barnes et al. (2018)). Bolded values indicate layers overlapping with Noah.

	Layer Number	Layer Thickness (m)	Depth Below Land Surface (m)	Heterogeneous Setup*	
				Porosity (–)	Hydraulic Conductivity (m/h)
Soil	1-3	0.1, 0.3, 0.6	0–1	0.45	0.0227
Impervious	1-3	0.1, 0.3, 0.6	0–1	0.05	0.00212
Saprolite	4–9	1, 1, 2, 2, 4, 4	1–15	0.45	0.00556
Transition Zone	10	4	15–19	0.45	0.227
Bedrock	11–12	4, 8	19–31	0.001	0.00001

<sup>\*</sup>For homogeneous scenarios, a porosity value of 0.434 and a hydraulic conductivity value of 0.0188 m/h. were used for the entire domain.

enable downscaling from low-resolution NARR atmospheric input data. Since high-resolution horizontal simulation of the atmospheric component was of interest (90-m grid resolution) at least five domains were needed to downscale boundary and initial conditions (BC and IC). Parent grid ratios were 3, 3, 5, and 3, respectively. All domains had 14,400 grid points in the horizontal plane. The 270-m LES domain helps spin up turbulence in the inflow from the 1350-m domain where turbulence is absent (parameterized), to the 90-m domain of interest (Mirocha et al., 2013).

To spin up and downscale input data for the WRF domains, the top three domains were run in one-way nesting mode starting 4 days prior to the start of the period of interest (July 15th, 2008). Ndown, a WRF tool providing offline interpolation schemes for downscaling from a parent domain to a child domain nested inside it, was then used to downscale the IC and BC from domain 3 to domain 4. Next, domain 4 was run in LES mode from July 18 to July 23. An extra day prior to the period of interest, in the simulation of domain 4 provides enough time for development of turbulent structures before the analysis period. The time step used in the domain 4 simulation was 0.5 s. Lastly, to run domain 5, again ndown was used to provide IC and BC from domain 4. The time step used for domain 5 simulations was 1/6 s. As mentioned above, the first 4 h of the domain 5 simulations were also considered as an additional spin-up period to allow the finest turbulence structure and the land surface to equilibrate.

The following physical schemes were used in all simulations with WRF: (1) Single-Moment 6-class scheme for microphysics option; (2) Rapid Radiative Transfer Model for longwave radiation; and (3) Dudhia scheme for shortwave radiation. For the three mesoscale simulations with grid resolutions larger than 1 km, the Yonsei University (Hong et al., 2006) planetary boundary layer (PBL) scheme was used, along with the 2D Smagorinsky scheme for horizontal diffusion. In LES simulations these schemes were turned off since turbulence was explicitly resolved on the model grids, and the 3D turbulent kinetic energy (TKE) model was used to parametrize subgrid-scale stresses and fluxes (as in Talbot et al., 2012).

# 2.2.5. Homogenous setup

The first series of simulations incorporated homogeneous subsurface hydrogeological properties. ParFlow has a 3D, variably saturated subsurface component with an integrated 2D overland flow component. Noah does not have any representation of lateral subsurface or overland surface flows. The homogeneous setup allowed isolating the effect of difference in the terrestrial hydrology parameterization in the two models (WRF-PUCM-PF vs WRF-PUCM).

For this set of simulations, ParFlow-CLM stand-alone spin-up simulations were conducted using hydraulic conductivity and porosity values of  $0.0188 \text{ m hr}^{-1}$  and 0.434, respectively. These values correspond to the dominant soil category (sandy loam) for the domain assigned by WRF Preprocessing System (WPS). All 12 subsurface layers in WRF-PUCM-PF and all four layers WRF-PUCM

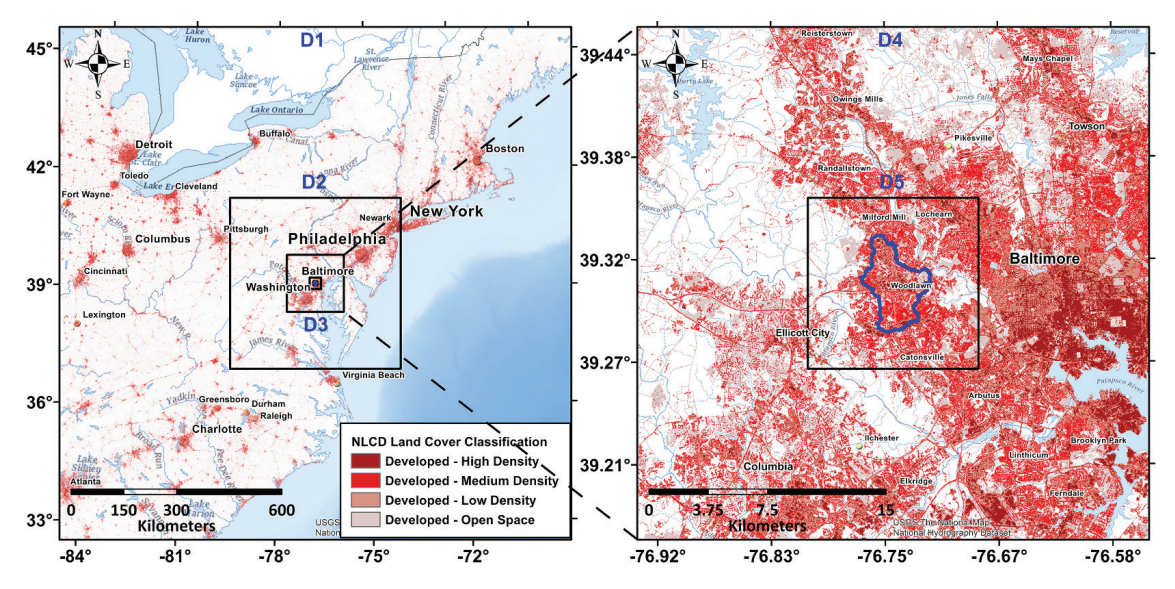


Fig. 3. Domains 1-5 are used for downscaling atmospheric BC and IC.

(Table 1) used these values in the homogeneous setup. Three-dimensional arrays of the final soil moisture content spun up in ParFlow were manually injected into an identical initial condition file for both WRF-PUCM and WRF-PUCM-PF simulations.

# 2.2.6. Heterogeneous setup

The full potential of the new model was demonstrated by incorporation of 3D subsurface hydrogeological properties in WRF-PUCM-PF. Such implementation enables representation of spatially variable values of hydraulic conductivity and porosity, particularly for impervious surfaces, which are important drivers of hydrology in urban areas.

We compared WRF-PUCM employing Noah's subsurface 2D heterogeneous soil properties as available in WPS, with WRF-PUCM-PF employing ParFlow's 3D heterogeneous soil properties based on literature values specific to the region. Table 1 lists the subsurface 3D hydraulic conductivity and porosity values used in the WRF-PUCM-PF setup. The top four layers' depths, shown in bold in the table, correspond to Noah's top four subsurface layer depths. The top 3 layers have two different sets of values associated with impervious and pervious land cover. These values are based on physically realistic values derived from literature by Barnes et al. (2018). For the WRF-PUCM simulation, 2D heterogeneous soil properties were generated by WPS, derived from low-resolution U.S. Department of Agriculture's State Soil Geographic Database. These categories do not include any representation for impervious surfaces. Therefore, the values captured from the soil categories maps by WPS represent the whole column. Although 2D hydrogeological properties of WRF-PUCM could be altered to get closer to the more physically realistic 3D values in ParFlow, this was intentionally avoided to allow comparison between the WRF-PUCM-PF with WRF-PUCM as it was originally used over urban areas. This comparison therefore includes both the improved subsurface physical representation as well as the improved characterization of subsurface hydrogeological properties.

Similar to the homogeneous setup, the stand-alone heterogeneous ParFlow-CLM simulations were run with the same atmospheric forcing conditions. Then the 3D spun-up volumetric soil moisture field was injected into both WRF-PUCM and WRF-PUCM-PF as initial conditions. Considering the homogeneous and heterogeneous setups for WRF-PUCM and WRF-PUCM-PF models, there were four test case scenarios evaluated (Table 2).

# 2.2.7. Computational resources

Stand-alone ParFlow spinup simulations were carried out on a local Dell Precision Tower 7910, using 16 processors. All WRF-PUCM and WRF-PUCM-PF spinups and final simulations were conducted on the high-performance computing Cheyenne system provided by NCAR's Computational and Information Systems Laboratory (2019). Simulations run on Cheyenne used 64 processors and required ~290,000 core-hours.

# 3. Results and discussion

To evaluate the performance of each model for both homogeneous and heterogeneous setups, we first examined the depth of precipitation generated by each model as a function of time to ensure that any differences observed in the soil moisture spatiotemporal evolution were not caused by a difference in rain depths. For all four cases, there were negligible differences in the amount of area-averaged rain at each time step (Fig. 4). The spatial distribution of accumulated generated rainfall for the entire simulation over the domain is shown for homogeneous cases in Fig. 5. This is expected since only the smallest domain was altered to include PF, and the differences in surface fluxes over such a limited area should not influence large storm systems generating rainfall.

# 3.1. Homogeneous (HMG) setup

Fig. 6a–d shows the area-averaged soil moisture values in the top four layers, for the HMG-WRF-PUCM and HMG-WRF-PUCM-PF models. Area-averaged soil moisture stayed almost constant throughout the entire simulation in layers 3 and 4 (spanning 0.4–2 m depth below land surface), in the HMG-WRF-PUCM-PF simulation (Fig. 6 c, d). For the HMG-WRF-PUCM simulation, the soil moisture in layer 3 decreased by 0.03 ( $\sim$ 11%) up to hour 96 and gained almost 0.02 ( $\sim$ 8%) toward the end of the simulation in response to heavy rain events during the last 24 h of simulation. In addition, soil layer 4 in HMG-WRF-PUCM lost almost 0.02 ( $\sim$ 7%) toward the end of the simulation.

For the top two layers (top 40 cm, Fig. 6 a, b) the evolution of soil moisture in response to rain was different. Up to the middle of simulation, when the first rain event occurs, layers 1 and 2 in HMG-WRF-PUCM lose 0.01 and 0.02 in soil moisture content; in HMG-WRF-PUCM-PF values are almost constant for these two layers. Fig. 7 shows this difference more starkly in space. Initially, both models have similar spatial soil moisture distributions. However, at hour 40, before the first rain, the HMG-WRF-PUCM case has lower soil moisture content near the stream network. The stream network has changed from red (associated with values above 0.4) to yellow

**Table 2**Designation of scenario runs.

No.	Case Name	Subsurface hydrogeology setup	Model
1	HMG-WRF-PUCM	Homogeneous	WRF-PUCM
2	HMG-WRF-PUCM-PF	Homogeneous	WRF-PUCM-PF
3	HTRG-WRF-PUCM	Heterogeneous 2D in Noah	WRF-PUCM
4	HTRG-WRF-PUCM-PF	Heterogeneous 3D in ParFlow	WRF-PUCM-PF

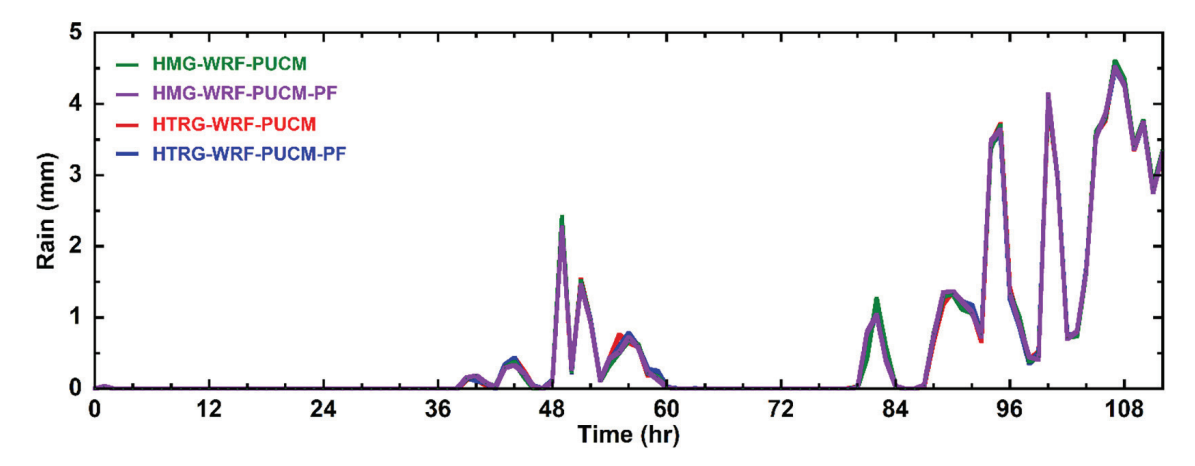


Fig. 4. Area-averaged hourly accumulated precipitation for four test case scenarios where HMG stands for homogeneous hydrogeology and HTRG stands for heterogeneous hydrogeology.

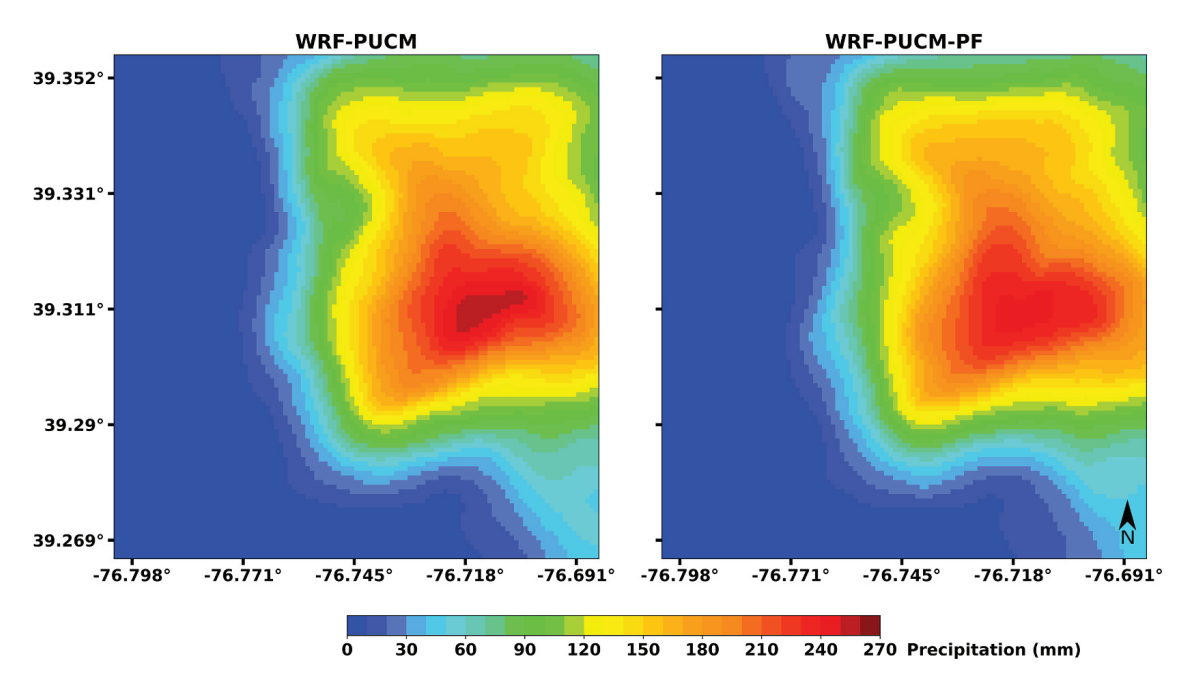


Fig. 5. Accumulated rain throughout the entire simulation time. Left: WRF-PUCM; right: WRF-PUCM-PF (both homogeneous cases). The rain distribution for the heterogeneous cases was not discernably different and therefore is not shown.

(associated with values between 0.28 and 0.32). The cells in the stream network in HMG-WRF-PUCM-PF remained nearly saturated in most places along the network (as expected). These changes are more apparent in animations of temporal evolution of contour plots of soil moisture distribution for different soil layers provided in Supplementary Movie 1.

To analyze the reason behind the loss of soil moisture in HMG-WRF-PUCM simulations in the first 40 h, we compared the spatiotemporal evolution of soil moisture among the four layers. Hourly snapshots of soil moisture distribution contour plots (Supplementary movie 1) revealed that after the start of the simulation, the riparian zones, which were fully saturated at a soil moisture value of 0.434, were draining quickly from the top to the bottom layers in HMG-WRF-PUCM simulation, but not in the simulations with PF. This is likely because ParFlow's integrated overland and subsurface flow components route water in the streams; the ponded pressure keeps soil layers below the streams fully saturated and reduces downward drainage. However, in HMG-WRF-PUCM, Noah uses the Simple Water Balance (SWB) model (Schaake et al., 1996) to calculate surface runoff, which is not routed horizontally.

The trends changed after the start of a rain event at hour 40 when HMG-WRF-PUCM infiltrates water faster than HMG-WRF-PUCM-PF. While area-averaged soil moisture content increased by almost 0.1 and 0.07 in layers 1 and 2 in HMG-WRF-PUCM, the corresponding values in WRF-PUCM-PF are 0.06 and 0.04. We examined the difference in spatial distribution of soil moisture content in both models. In the middle of the simulation (Fig. 7b), the soil moisture level is higher in HMG-WRF-PUCM-PF compared to HMG-WRF-PUCM. This is more obvious when looking at the difference contour map in Supplementary Fig. 1, where the difference between soil moisture at each cell between HMG-WRF-PUCM and HMG-WRF-PUCM-PF is illustrated. The difference appears to be

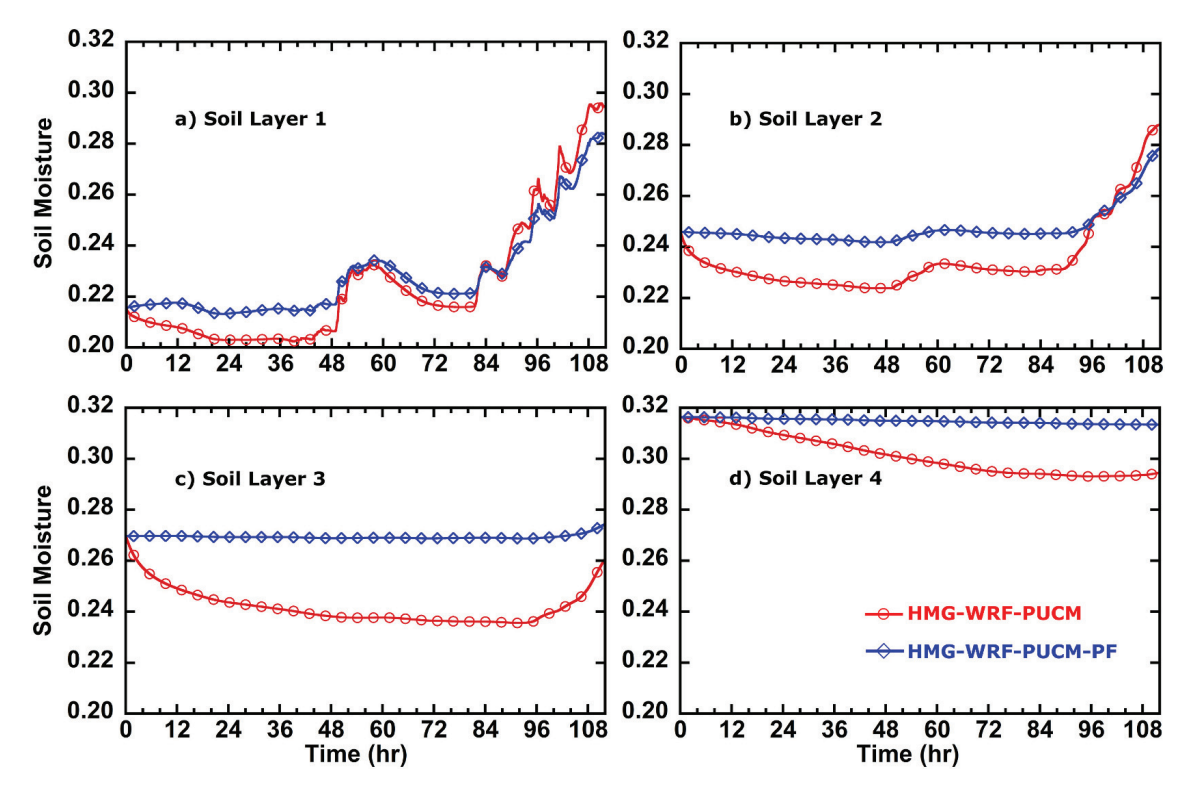


Fig. 6. Area-averaged soil moisture for the homogenous case scenarios with WRF-PUCM and WRF-PUCM-PF models. Soil moisture content temporal profiles in the top four layers of the soil are shown in a,b,c, and d.

reflective of the stream network pattern generated by ParFlow in spin-up simulations, as propagated through the HMG-WRF-PUCM-PF simulations.

While soil moisture increased in the first layer in HMG-WRF-PUCM-PF simulation, corresponding to the location of rain, the slopes and lateral overland and subsurface component of flow had a significant impact on the distribution. More specifically, saturated zones still closely mimicked the pattern of stream network or topographic pattern. Riparian zones, saturated throughout the entire simulation, widened, corresponding to increases in streamflow depths in response to rain events. On the west side of the domain where no rainfall occurred, cells associated with the stream network were fully saturated in HMG-WRF-PUCM-PF, whereas in HMG-WRF-PUCM soil moisture decreased to values between 0.26 and 0.32. This shows that in the HMG-WRF-PUCM scenario, soils in the stream network continued to lose a great amount of soil moisture, but at lower rates compared to the beginning of the simulation. High-resolution simulations enabled representation of hydrological processes closer to typically observed systems. For example, simulated stream networks generated by these simulations generally aligned with the geometry observed stream network. As emphasized in the introduction, this is important since variations in hydrometeorological processes of interest in urban areas occur at fine scales.

Next, to evaluate the effects of soil moisture difference on energy-water cycle parameters at the land surface and on microclimatic parameters, we examined patterns of latent heat flux (LHF) and land surface temperature (LST), depicted in Figs. 8 and 9, that show area-averaged LHF and LST throughout the entire simulation. It can be seen that LHF in both models is affected by soil moisture at the top layer (Fig. 8). The values of area-averaged LHF for both models are almost identical up to hour 12 of the simulation. Then between hours 16 to 20 (12 PM to 4 PM ET), when the incoming solar radiation is at its highest value, the output from HMG-WRF-PUCM shows almost a  $10 \text{ W m}^{-2}$  lower LHF compared to HMG-WRF-PUCM-PF. Lower LHF in HMG-WRF-PUCM can be explained as a result of lower soil moisture availability in parts of the top layer associated with the stream network (Supplementary Fig. 1). In contrast, during rain events and at the end of the simulation where HMG-WRF-PUCM reached higher soil moisture content compared to HMG-WRF-PUCM-PF, HMG-WRF-PUCM has higher LHF. The peak of the area-averaged LHF difference occurs between hours 86 and 94, corresponding to 10 AM and 10 PM, reaching 10 PM and  $10 \text{ PM$ 

As expected, the LST time series mirrors its LHF counterpart, with lower surface temperatures corresponding to higher LHF and vice-versa (Fig. 9). From the middle of the simulation toward the end of the simulation at periods with a large difference in LHF (hour 84–96), the output from HMG-WRF-PUCM is almost 1 °C cooler on average over the domain than HMG-WRF-PUCM-PF. To further investigate the difference between the LST generated by the two models, we evaluated contour maps of LST spatial distribution at hour 50, 10 PM ET on July 20 (Fig. 10). At this time the two models reached one of their greatest differences in LHF (Fig. 8). Fig. 10 shows the contour plots of both soil moisture and LST at this time. The northeast part of the domain in WRF-PUCM has higher soil moisture content compared to WRF-PUCM-PF, resulting in cooler LSTs in that part. This difference is further clarified in Supplementary Fig. 2, which is a contour plot of differences. As can be seen over the northeast part of the domain, the difference between LST between the two domains ranges from  $\approx 1.5$  to 3.0 °C. This difference over this area extent could have a considerable impact on water and energy balances at the land surface, as well as on human thermal comfort.

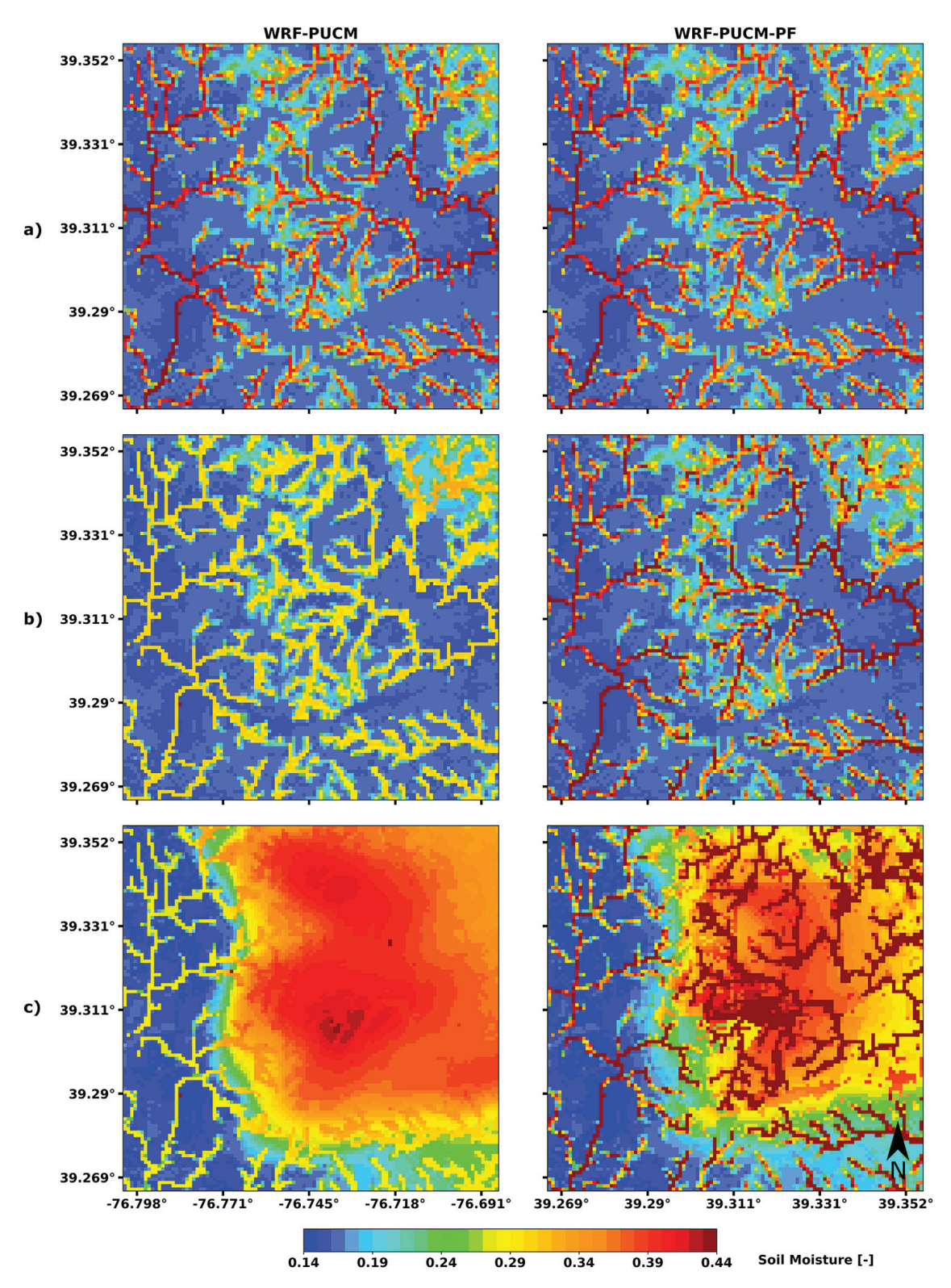


Fig. 7. Contour plots of soil moisture distribution in the first soil layer in HMG-WRF-PUCM (left) and HMG-WRF-PUCM-PF (right). a) start of the simulation; b) at hour 40 of the simulation before the first rain event; c) at the end of the simulation at hour 112.

# 3.2. Heterogeneous setup

The heterogeneous scenarios started with an initial soil moisture distribution that was spun up in stand-alone mode with ParFlow-CLM, in a separate setup. As a result, heterogeneous initial area-averaged soil moisture was around 0.07 compared to the homogeneous initial value around 0.22. Although the atmospheric forcing used in the spin-up was the same used for the stand-alone homogeneous

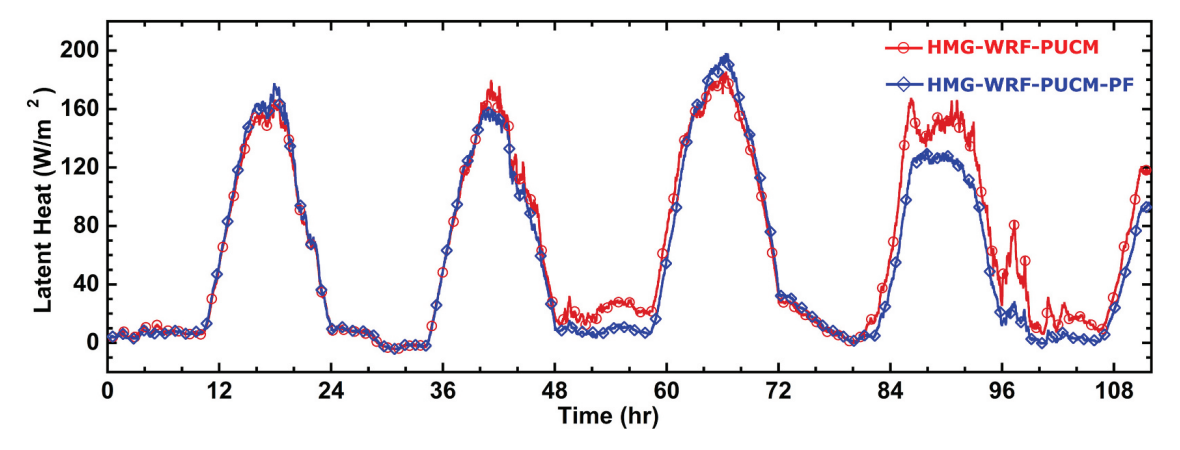


Fig. 8. Area-averaged latent heat flux for the homogeneous setup cases.

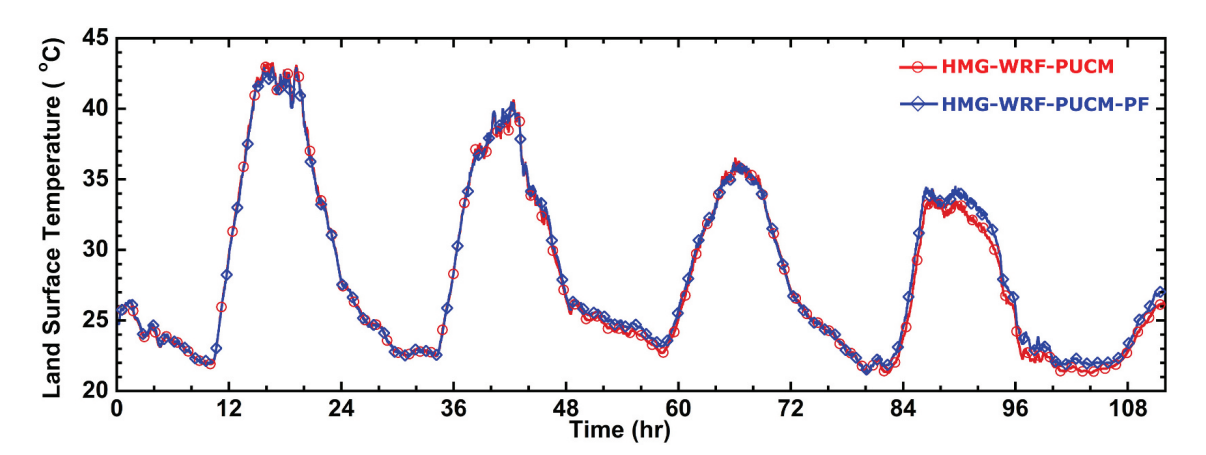


Fig. 9. Area-averaged land surface (skin) temperature for the homogeneous setup cases.

case, implementation of impervious surfaces representation resulted in lower domain-averaged subsurface storage at the end.

Similarity of area-averaged rainfall (Fig. 4) amount allows cross-comparison between homogeneous and heterogeneous case scenarios to isolate any effects of geologic heterogeneity. Fig. 11 shows the area-averaged soil moisture time series for the heterogeneous case scenarios. Layers 3 and 4 have almost constant area-averaged soil moisture content throughout the entire simulation, for both models. In HTRG-WRF-PUCM the two layers lose a small amount of water due to the low rate of free drainage in Noah. In HTRG-WRF-PUCM-PF, layers 3 and 4 appear to gain small amounts of water in the last 16 h of simulation in response to the heavy rain event occurring at the end of the simulation.

Higher area-averaged soil moisture at layer 4 ( $\sim$ 0.3), almost three times the value of other layers at the beginning of the simulation, is due to the higher hydraulic conductivity and porosity values associated with the saprolite layer, compared to layers 1–3 being associated with lower values (Table 1). Under stand-alone spin-up simulations with ParFlow, soils in layers below impervious surfaces reached higher soil moisture content compared to the top layers (layers 1–3) due to lateral subsurface inflow. As shown by Barnes et al. (2018), this is because, during stand-alone simulations, water can seep through the subsurface domain laterally and flow beneath impervious surfaces. Moreover, this water is later prevented by the top impervious layers from exiting the domain vertically, resulting in a more saturated condition compared to the layers above. The increase in area-averaged soil moisture content, in layers 1 and 2 for HTRG-WRF-PUCM-PF is small ( $\sim$ 0.02 and  $\sim$ 0.01). These values are six and four times smaller than the values in homogeneous layers, corresponding to low hydraulic conductivities of impervious surfaces and low porosity values for the top three soil layers (Table 1).

For HTRG-WRF-PUCM, the final increases in area-averaged soil moisture in layers 1 and 2 are 0.18 and 0.10. These final values are twice the values observed in the homogeneous setup. The higher increase in HTRG-WRF-PUCM soil moisture is due to lower initial soil moisture content. The drier soil in the heterogeneous case gains and retains more water from rainfall compared to the homogeneous case. More importantly, the increase in area-averaged values of soil moisture in the top two layers HTRG-WRF-PUCM are 9 to 10 times the values observed in HTRG-WRF-PUCM-PF simulations. This difference is caused by a combination of higher surface runoff in the HTRG-WRF-PUCM-PF simulations, associated with impervious surfaces; and higher infiltration rates in HTRG-WRF-PUCM associated with Noah's implementation of hydrology (no overland flow; Appendix A) and 2D geologic properties. Noah's 2D geologic properties are based on 16-category soil categories developed at a 1-km grid resolution, and no category exists for impervious surface parameterization.

Fig. 12 shows contour plots of soil moisture distribution at the start and end of the simulation for both heterogeneous models. The

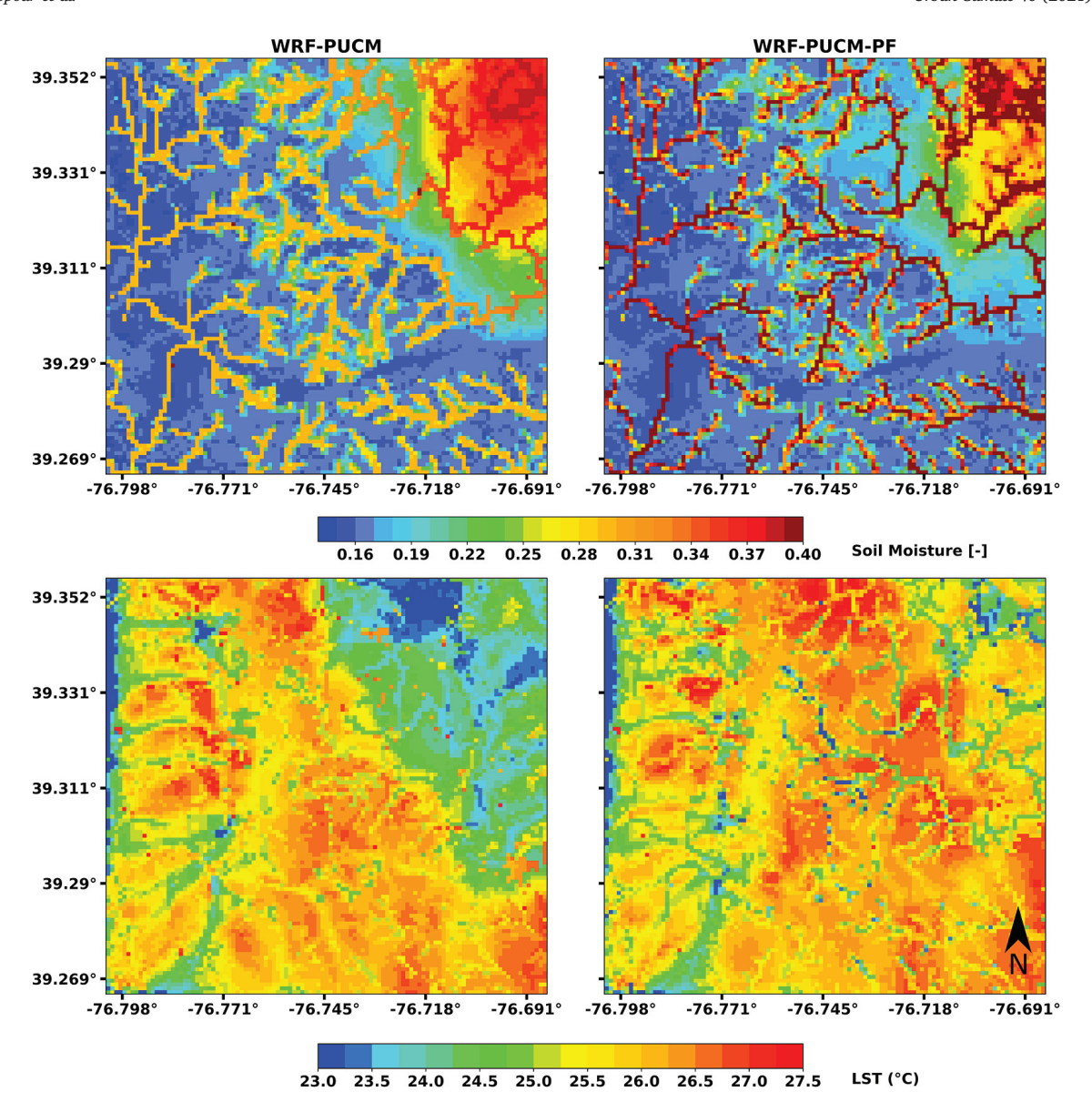


Fig. 10. Soil moisture at the land surface and land-surface temperature contour plots at hour 50 (July 20 @ 10 PM) for homogeneous simulations.

similarity of soil moisture contours in HTRG-WRF-PUCM at the end of the simulation (Fig. 12-b) to contours of the spatial distribution of accumulated rainfall for the entire simulation (Fig. 5) is apparent. It demonstrates: (1) the lack of lateral component of flow in HTRG-WRF-PUCM simulation; and (2) the fact that HTRG-WRF-PUCM allows water to infiltrate at high rates over areas that are covered by impervious surface, but may not be represented as such. Although representation of impervious surfaces is implemented in PUCM for calculation of the surface energy budget through high-resolution land cover maps, subsurface hydrogeologic representation of impervious surfaces in Noah is not included. Therefore, soil moisture in cells receiving rainfall increased from values below 0.05 (blue in Fig. 12-a, left side) to values between 0.25 and 0.45 (blue in Fig. 12-b, left side).

In the HTRG-WRF-PUCM-PF output, a much smaller area under the rain location had an increase in soil moisture. More importantly, most of the cells that had increased soil moisture had a lower rise compared to HTRG-WRF-PUCM. While most of the cells in HTRG-WRF-PUCM under the rainfall area gained soil moisture increases of around 0.2 to 0.35, the increase in HTRG-WRF-PUCM-PF was around 0.05 (Fig. 12). Nevertheless, cells in the riparian zones had higher increases and were saturated. Also, there was a large approximately circular area on the central east side of the domain, which turned yellow, corresponding to around 0.2 increase in soil moisture content values. Further investigation indicated that the area corresponds to Leakin Park which is situated at a valley in Baltimore City. This park location is shown in Fig. 2.

Figs. 13 and 14 show area-averaged LHF and LST output for both models with the heterogeneous setup. Before the start of rain events, since soil moisture content for both models is similar in the first soil layer (Fig. 11a), the LHF and LST were similar. However, with the start of rain and higher infiltration rates in HTRG-WRF-PUCM compared to HTRG-WRF-PUCM-PF, the LHF in HTRG-WRF-PUCM increased by 25–40% (140 W  $\rm m^{-2}$ ) toward the end of the simulation between hours 84 and 96. In turn, the increase in area-averaged LHF in HTRG-WRF-PUCM resulted in 2  $\rm ^{\circ}C$  area-averaged cooler surface temperatures compared to HTRG-WRF-PUCM-PF,

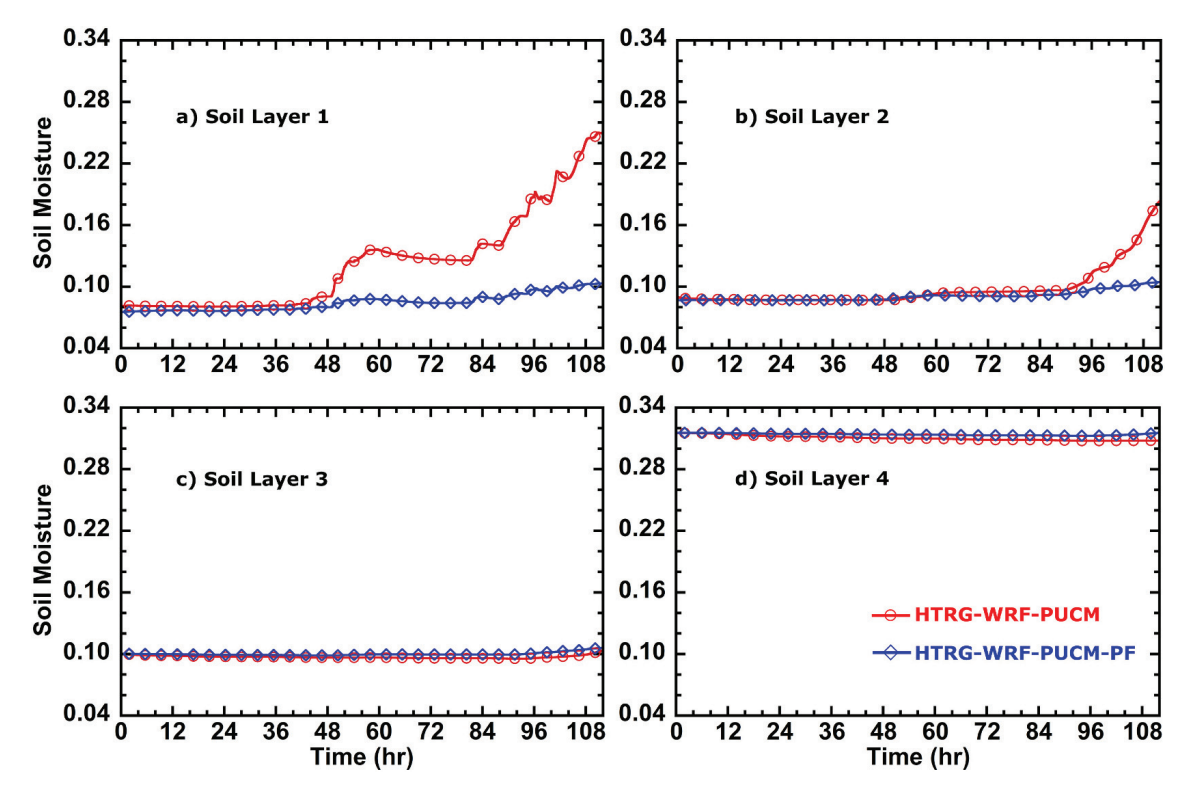


Fig. 11. Area-averaged soil moisture for the homogenous case scenarios with HTRG-WRF-PUCM and HTRG-WRF-PUCM-PF models. Soil moisture content temporal profiles in the top four layers of the soil for heterogeneous cases are shown in a, and b respectively.

between hours 86 to 90.

To further investigate the difference between the surface temperature distribution we evaluated contour plots of differences between LST at each cell for the two models. Fig. 15 demonstrates this difference at hour 92, corresponding to the greatest difference in area-averaged LST and LHF between the two models (Figs. 13 and 14). As can be seen in most of the areas corresponding to the precipitation (Fig. 5), HTRG-WRF-PUCM-PF had a higher temperature compared to HTRG-WRF-PUCM. The values for each cell represent the values of HTRG-WRF-PUCM-PF minus the values of WRF-PUCM. Other than some small patches that correspond to the large park on the east side of the domain at the lowest elevation, most areas rained on had temperature differences between 6 and 10 °C. The park area at which HTRG-WRF-PUCM-PF had lower temperatures (or where the values of difference were negative), is associated with higher soil moisture content due to the overland flow component of ParFlow. Overall, the difference in soil moisture distribution was mainly caused by different terrestrial hydrology representations by ParFlow and had significant impacts on LHF and LST over urban areas. This is most obvious after rain events.

# 4. Conclusions

This study developed and tested a new fully-coupled atmosphere-land surface-subsurface model (WRF-PUCM-PF) for the study of urban hydrometeorological processes at high resolutions. We applied WRF-PUCM-PF and WRF-PUCM models (using WRF in the LES mode) to a small urban watershed (Dead Run), located in suburban Baltimore, Maryland, USA for the purpose of generating example output using realistic input data. To isolate the effect of terrestrial hydrologic parameterization in the two models from the effect of differences in subsurface hydrogeologic properties on soil moisture distribution between the two models, we first applied the two models to domains with homogeneous subsurface properties. Next, we applied both models to domains with heterogeneous subsurface properties, to highlight differences in predictions of the two models with a more realistic representation of geologic properties. These tests aimed to verify that WRF-PUCM-PF produces realistic soil moisture and temperature distributions and to test if it would significantly alter urban hydrometeorological simulation compared to WRF-PUCM. The following are summary remarks based on the four simulations run with both models:

- In both homogeneous and heterogeneous simulations, the spatial distribution of soil moisture for the WRF-PUCM model at the last time step was similar to the spatial distribution of accumulated rain for the entire simulation. Areas under higher accumulated rain corresponded to areas of higher soil moisture content, while stream networks were completely unnoticeable. This highlighted a limitation of Noah, which is constrained to model only vertical flows.
- Although the homogeneous WRF-PUCM-PF spatial distribution of soil moisture had the signature of the spatial distribution of accumulated rain at the end of the simulation, the effect of the overland flow component could be easily seen. The higher soil

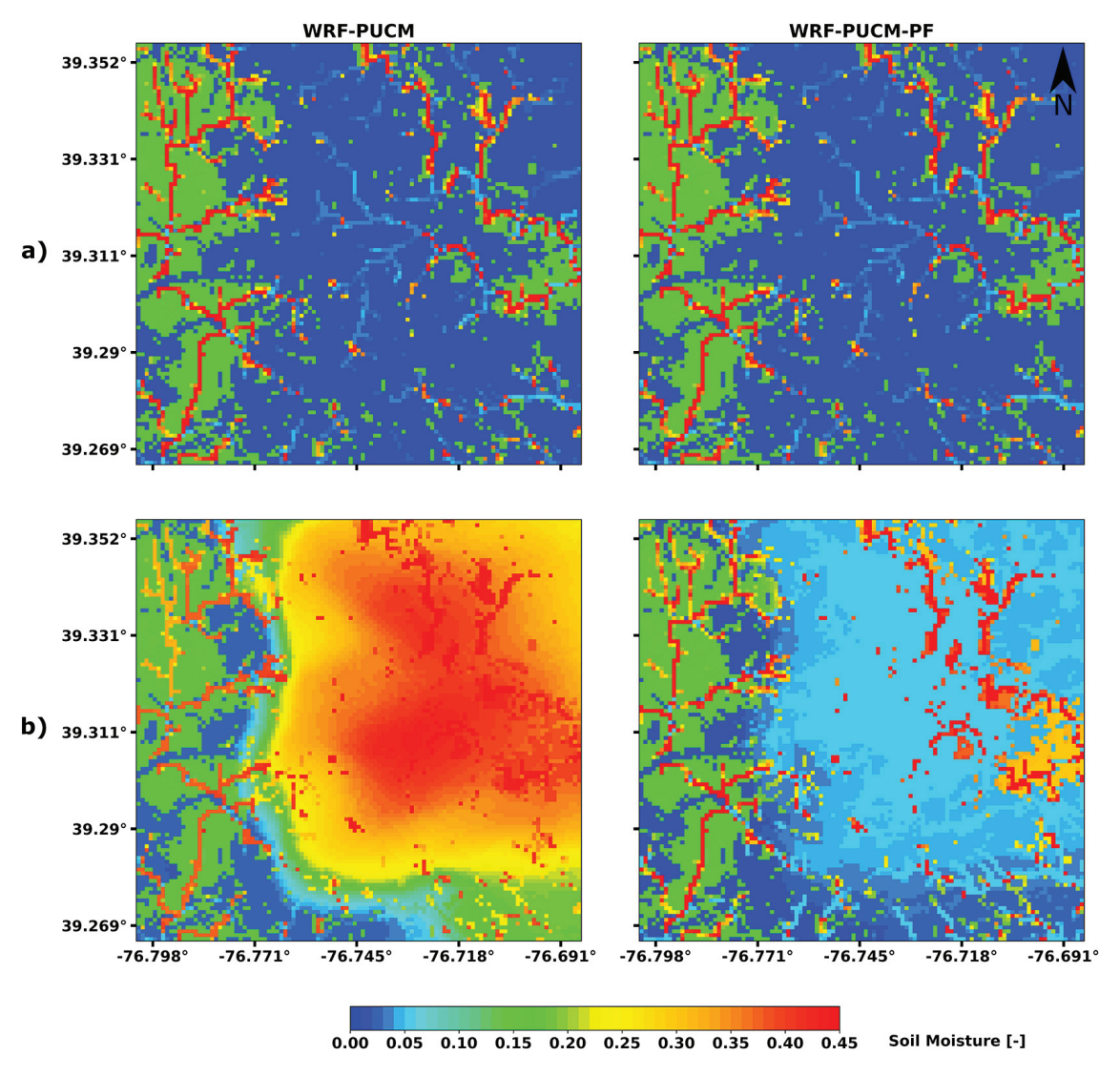


Fig. 12. Contour map plots of soil moisture distribution in the first soil layer in HTRG-WRF-PUCM and HTRG-WRF-PUCM-PF. a) start of the simulation; b) at the end of the simulation at hour 112.

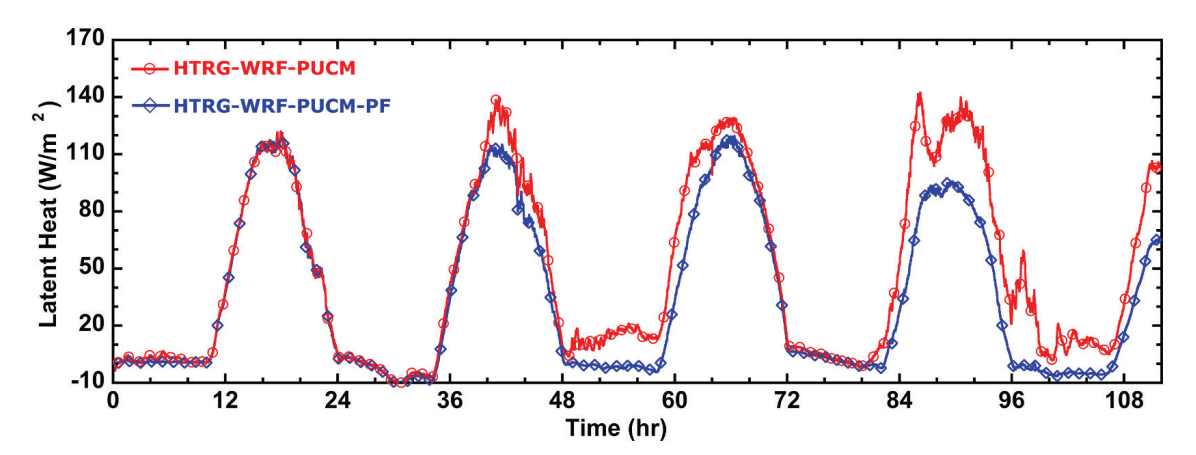


Fig. 13. Area-averaged LHF for the heterogeneous setup cases.

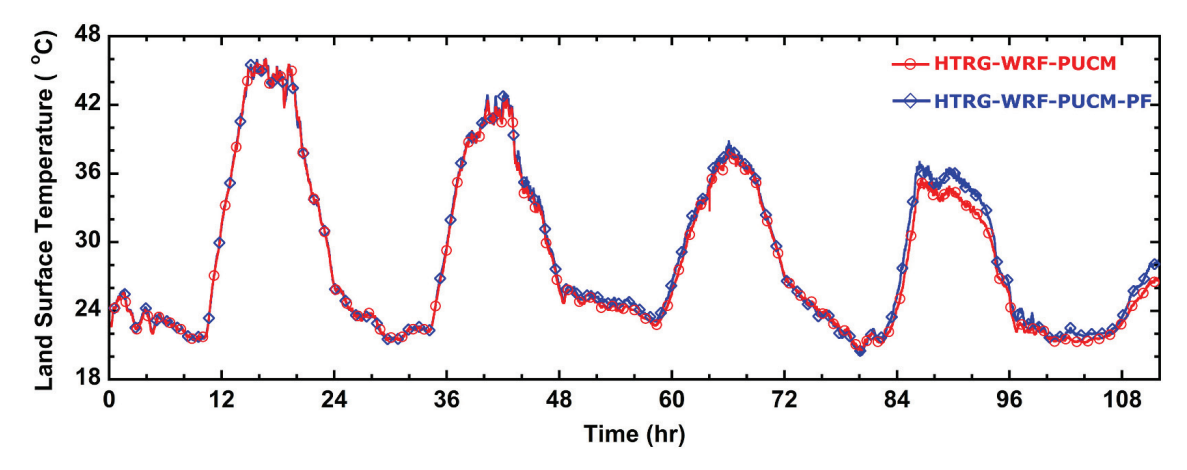


Fig. 14. Area-averaged LST for the heterogeneous setup cases.

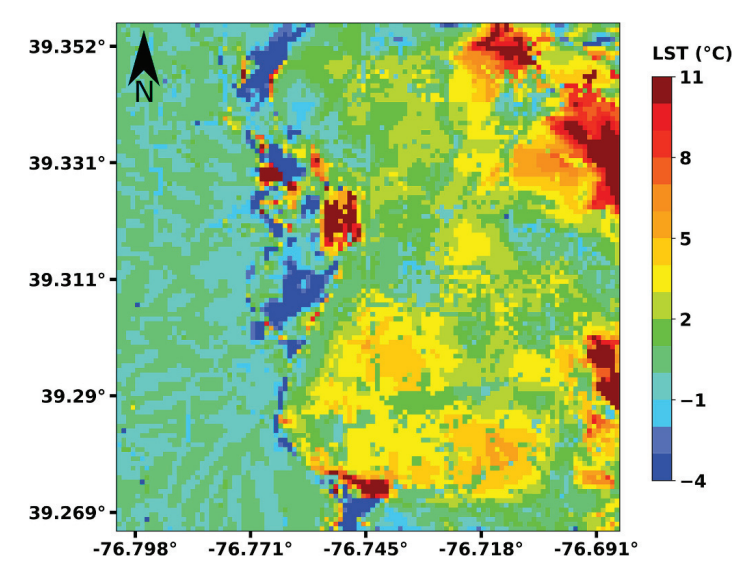


Fig. 15. Contour maps of the spatial distribution of LST difference (WRF-PUCM-PF minus WRF-PUCM) for the heterogeneous setups between the two models on July 22 at 4 PM (hour 92).

moisture content was associated with stream networks, riparian zones, and valleys. On the other hand, the heterogeneous WRF-PUCM-PF run, incorporating heterogeneous geologic properties, had a lower soil moisture gain compared to the homogeneous WRF-PUCM-PF run. Impervious surface implementation in the subsurface properties of the domain resulted in most of the rain generating runoff. Only stream networks at lower elevations that had permeable soils gained higher soil moisture.

• The difference in soil moisture distribution between WRF-PUCM and WRF-PUCM-PF, in both homogeneous and heterogeneous scenarios, led to differences in latent heat flux and land surface temperature spatiotemporal distributions. The differences in the heterogeneous simulations were greater since the two simulations also differed in the hydrological properties of the subsurface domain. During the dry-down period up to the middle of the simulation at hour 40, the heterogeneous simulations of both HTRG-WRF-PUCM and HTRG-WRF-PUCM-PF had a similar spatiotemporal distribution of LHF and LST. After hour 40 when rain events started, due to higher soil moisture availability in HTRG-WRF-PUCM compared to HTRG-WRF-PUCM-PF, the spatiotemporal LHF and LST diverged, specifically during daytime when incoming solar radiation reaches its highest intensity around noon. More specifically, the largest difference could be seen between hours 92 and 96 (12 PM and 4 PM locally), where the LST discrepancy over urban land cover for HTRG-WRF-PUCM-PF is 6 to 10 °C higher compared to HTRG-WRF-PUCM simulation. Such differences would significantly alter thermal comfort and the health and energy impacts of the urban heat island, as well as the hydrometeorology of any subsequent rainfall.

Building upon WRF-PUCM and ParFlow-WRF, with improved representation of urban heterogeneous energy and water fluxes, the new model enhanced representation of urban hydrometeorological processes. More importantly, WRF-LES enabled capturing the hydrometeorological processes influenced by fine-scale hygrothermal variation resulting from the highly heterogeneous urban land cover. Overall, the soil moisture distribution influenced by lateral overland flow over impervious surfaces turning to runoff is qualitatively closer to reality. The goal was to first evaluate how distinct the WRF-PUCM-PF simulated hydrometeorological fields could be

relative to the original WRF-PUCM model. Since isolation of each part of the hydrologic representation was the goal, several case scenarios were designed with a relatively small domain to allow us to run a suite of scenarios in a computationally efficient way. Moreover, as the goal was to compare the two models using identical input data, no comparison of model output to field data was done. However, validation is essential to demonstrate that the addition of the subsurface model not only makes the output fields more realistic, but that it has an appreciable impact on the model prognostic skill. Given the significant difference WRF-PUCM-PF had in this small domain, future model evaluation work can focus on exploring how soil moisture conditions and microclimatic parameters compare to real data under different conditions.

The high-resolution that our fully-coupled model captures could also be helpful to examine microclimatic variations in cities over different urban land covers at much finer grid resolutions, as well as how the mean flow field and turbulence respond to the land forcing. This is a benefit of using the large-eddy simulation technique that was not fully exploited in this study. Moreover, better representation of hydrometeorological variations from urban to rural areas, and inclusion of groundwater processes could be used to improve the evaluation of UHI and its various mitigation strategies, as well as its interactions with groundwater in places with shallow groundwater.

Supplementary data to this article can be found online at https://doi.org/10.1016/j.uclim.2021.100985.

# **Declaration of Competing Interest**

The authors declare that they have no known competing financial interests or personal relationships that could have appeared to influence the work reported in this paper.

# Acknowledgments

This work was supported by the Urban Water Innovation Network under National Science Foundation Cooperative Agreement #1444758. The simulations were conducted on the high-performance computing Cheyenne system (doi:https://doi.org/10.5065/D6RX99HX) provided by NCAR's Computational and Information Systems Laboratory and sponsored by National Science Foundation. We would like to acknowledge NCAR's staff computational and administrative support throughout this project. We would like to also acknowledge UMBC's unlimited storage on Google Drive which has helped manage our data. Transferring data between Google Drive and Cheyenne would not be possible without the Rclone project (https://rclone.org/). We are also grateful for helpful discussions with Michael Barnes, Mary Forrester, Mohammad Heidarinejad, Dan Li, Jiachuan Yang, Theodore Lim, Reed Maxwell, and Alimatou Seck.

# Appendix A. Implementation of terrestrial hydrology

Formulations for terrestrial hydrology incorporated into the coupled codes have been published elsewhere but are summarized here for the convenience of the reader.

# A.1. ParFlow configuration of terrestrial hydrology

In WRF-PUCM-PF, ParFlow models integrated surface-subsurface terrestrial hydrology. ParFlow is a three dimensional, variably-saturated groundwater model (Ashby and Falgout, 1996; Jones and Woodward, 2001; Maxwell, 2013), with an integrated overland flow component, represented through a boundary condition derived from the application of continuity condition for pressure and flux (Kollet and Maxwell, 2006). ParFlow solves the Richards (Richards, 1931) equation to model the variably-saturated subsurface hydrology:

$$S_S S_W \frac{\partial h}{\partial t} + \phi \frac{\partial S_W(h)}{\partial t} = \nabla \cdot \mathbf{q} + q_r(x, z) \tag{A.1}$$

where  $S_S$  is specific storage  $[L^{-1}]$ ;  $S_W$  is relative saturation [-]; h is pressure head [L]; t is time [T];  $\phi$  is porosity [-]; q is Darcy flux  $[LT^{-1}]$ ;  $q_r$  is the general source/sink term that represents fluxes including rainfall, transpiration, wells, and irrigation  $[LT^{-1}]$ . The Darcy flux is expressed as:

$$\mathbf{q} = \phi S_W(h)\mathbf{v} = -\mathbf{K}_S(x)k_r(h)\nabla(h+z) \tag{A.2}$$

where  $\mathbf{v}$  is subsurface velocity [LT<sup>-1</sup>];  $\mathbf{K}_S$  is saturated hydraulic conductivity tensor [LT<sup>-1</sup>]; and  $k_r$  is relative permeability [–]. ParFlow's integrated overland flow component is represented through a boundary condition derived from the application of continuity condition for pressure and flux (Kollet and Maxwell, 2006), and expressed as the two-dimensional kinematic wave equation:

$$\mathbf{k}(-\mathbf{K}_{S}(\mathbf{X})k_{r}(h)\nabla(h+z)) = \frac{\partial \|h,0\|}{\partial t} - \nabla \cdot \|h,0\|\mathbf{v}^{SW} + q_{r}(x)$$
(A.3)

where **k** is a unit vector in the vertical direction [-], and *h* is surface ponding depth [L]. ||h,0|| picks the maximum of *h* or zero, resulting in equivalency between surface ponding and pressure head in Eq. A.1 when h > 0.  $q_r(x)$  is also equivalent to the source/sink term in Eq. A.1 but at the surface. This boundary condition is based on the assumption that surface pressure and ponding depth are the

same at the ground surface.

## A.2. Noah configuration of terrestrial hydrology

In WRF-PUCM, Noah is used for modeling the terrestrial hydrology processes. Noah was developed as an LSM and coupled to WRF as an atmospheric model for mesoscale applications (Chen and Dudhia, 2001). In those applications, grid resolutions were coarse, on the order of several kilometers. Therefore, lateral surface and subsurface flow effects were negligible. For those applications, Chen and Dudhia (2001) implemented the simplistic one-dimensional Richards equation:

$$\frac{\partial \Theta(h)}{\partial t} = \frac{\partial}{\partial z} \left( D \frac{\partial \Theta}{\partial z} \right) + \frac{\partial K}{\partial z} + F_{\Theta} \tag{A.4}$$

where  $\Theta$  is soil moisture content [-]; D is the soil water diffusivity  $[L^2T^{-1}]$ , and K is the vertical hydraulic conductivity  $[LT^{-1}]$ .  $F_{\theta}$  is the general source/sink term for soil water that represents fluxes including rainfall, transpiration, wells, and irrigation  $[T^{-1}]$ . This version of the Richards equation is derived under the assumption that subsurface flow is one-dimensional vertical flow, rigid, and homogeneous.

Noah calculates runoff, R, as an excess of precipitation not infiltrated ( $R = P_d - I_{max}$ ). In this implementation, overland flow is not represented. Rather, at every timestep, surface runoff is computed and discarded from the domain. Therefore, lateral overland flow is not modeled.

# References

Ashby, S.F., Falgout, R.D., 1996. A parallel multigrid preconditioned conjugate gradient algorithm for groundwater flow simulations. Nucl. Sci. Eng. 124, 145–159. https://doi.org/10.13182/NSE96-A24230.

Barnes, M.L., Welty, C., Miller, A.J., 2016. Global topographic slope enforcement to ensure connectivity and drainage in an urban terrain. J. Hydrol. Eng. 21, 06015017 https://doi.org/10.1061/(ASCE)HE.1943-5584.0001306.

Barnes, M.L., Welty, C., Miller, A.J., 2018. Impacts of development pattern on urban groundwater flow regime. Water Resour. Res. 54, 5198–5212. https://doi.org/10.1029/2017WR022146.

Bhaskar, A.S., Welty, C., Maxwell, R.M., Miller, A.J., 2015. Untangling the effects of urban development on subsurface storage in Baltimore. Water Resour. Res. 51, 1158–1181. https://doi.org/10.1002/2014WR016039.

Block, A., Keuler, K., Schaller, E., 2004. Impacts of anthropogenic heat on regional climate patterns. Geophys. Res. Lett. 31 https://doi.org/10.1029/2004GL019852 n/a-n/a.

Bou-Zeid, E., Anderson, W., Katul, G.G., Mahrt, L., 2020. The persistent challenge of surface heterogeneity in boundary-layer meteorology: a review. Boundary-Layer Meteorol. 1–19. https://doi.org/10.1007/s10546-020-00551-8.

Chen, F., Dudhia, J., 2001. Coupling an Advanced land surface-hydrology model with the Penn State-NCAR MM5 modeling system. Part I: model implementation and sensitivity. Mon. Weather Rev. 129, 569–585. https://doi.org/10.1175/1520-0493(2001)129<0569:CAALSH>2.0.CO;2.

Dai, Y., Zeng, X., Dickinson, R.E., Baker, I., Bonan, G.B., Bosilovich, M.G., Denning, A.S., Dirmeyer, P.A., Houser, P.R., Niu, G., Oleson, K.W., Schlosser, C.A., Yang, Z.-L., 2003. The Common Land Model. Bullet. Amer. Meteorol. Soc. 84 (8), 1013–1024. https://doi.org/10.1175/BAMS-84-8-1013.

Fersch, B., Senatore, A., Adler, B., Arnault, J., Mauder, M., Schneider, K., Völksch, I., Kunstmann, H., 2020. High-resolution fully coupled atmospheric–hydrological modeling: a cross-compartment regional water and energy cycle evaluation. Hydrol. Earth Syst. Sci. 24, 2457–2481. https://doi.org/10.5194/hess-24-2457-2020. García-Sánchez, C., van Beeck, J., Gorlé, C., 2018. Predictive large eddy simulations for urban flows: challenges and opportunities. Build. Environ. 139, 146–156. https://doi.org/10.1016/j.buildenv.2018.05.007.

Hong, S.-Y., Noh, Y., Dudhia, J., 2006. A new vertical diffusion package with an explicit treatment of entrainment processes. Mon. Weather Rev. 134, 2318–2341. https://doi.org/10.1175/MWR3199.1.

Jones, J.E., Woodward, C.S., 2001. Newton–Krylov-multigrid solvers for large-scale, highly heterogeneous, variably saturated flow problems. Adv. Water Resour. 24, 763–774. https://doi.org/10.1016/S0309-1708(00)00075-0.

Kollet, S.J., Maxwell, R.M., 2006. Integrated surface–groundwater flow modeling: a free-surface overland flow boundary condition in a parallel groundwater flow model. Adv. Water Resour. 29, 945–958. https://doi.org/10.1016/j.advwatres.2005.08.006.

Kollet, S.J., Maxwell, R.M., 2008. Capturing the influence of groundwater dynamics on land surface processes using an integrated, distributed watershed model. Water Resour. Res. 44, 1–18. https://doi.org/10.1029/2007WR006004.

Li, D., Bou-Zeid, E., 2013. Synergistic interactions between urban Heat Islands and heat waves: the impact in cities is larger than the sum of its parts\*. J. Appl. Meteorol. Climatol. 52, 2051–2064. https://doi.org/10.1175/JAMC-D-13-02.1.

Li, D., Bou-Zeid, E., 2014. Quality and sensitivity of high-resolution numerical simulation of urban heat islands. Environ. Res. Lett. 9 https://doi.org/10.1088/1748-9326/9/5/055001.

Li, D., Bou-Zeid, E., Oppenheimer, M., 2014. The effectiveness of cool and green roofs as urban heat island mitigation strategies. Environ. Res. Lett. 9, 55002. https://doi.org/10.1088/1748-9326/9/5/055002.

Liu, Y.S., Miao, S.G., Zhang, C.L., Cui, G.X., Zhang, Z.S., 2012. Study on micro-atmospheric environment by coupling large eddy simulation with mesoscale model. J. Wind Eng. Ind. Aerodyn. 107–108, 106–117. https://doi.org/10.1016/J.JWEIA.2012.03.033.

Lopez, S.R., Maxwell, R.M., 2016. Identifying urban features from LiDAR for a high-resolution urban hydrologic model. JAWRA J. Am. Water Resour. Assoc. 52, 756–768. https://doi.org/10.1111/1752-1688.12425.

Manoli, G., Fatichi, S., Schläpfer, M., Yu, K., Crowther, T.W., Meili, N., Burlando, P., Katul, G.G., Bou-Zeid, E., 2019. Magnitude of urban heat islands largely explained by climate and population. Nature 573, 55–60. https://doi.org/10.1038/s41586-019-1512-9.

Manoli, G., Fatichi, S., Bou-Zeid, E., Katul, G.G., 2020. Seasonal hysteresis of surface urban heat islands. Proc. Natl. Acad. Sci. 117, 7082–7089. https://doi.org/10.1073/pnas.1917554117.

Mauree, D., Blond, N., Clappier, A., 2018. Multi-scale modeling of the urban meteorology: integration of a new canopy model in the WRF model. Urban Clim. 26, 60–75. https://doi.org/10.1016/j.uclim.2018.08.002.

Maxwell, R.M., 2013. A terrain-following grid transform and preconditioner for parallel, large-scale, integrated hydrologic modeling. Adv. Water Resour. 53, 109–117. https://doi.org/10.1016/j.advwatres.2012.10.001.

Maxwell, R.M., Miller, N.L., 2005. Development of a coupled land surface and groundwater model. J. Hydrometeorol. 6, 233–247. https://doi.org/10.1175/ JHM422.1.

Maxwell, R.M., Lundquist, J.K., Mirocha, J.D., Smith, S.G., Woodward, C.S., Tompson, A.F.B., 2011. Development of a coupled groundwater–atmosphere model. Mon. Weather Rev. 139, 96–116. https://doi.org/10.1175/2010MWR3392.1.

- Meili, N., Manoli, G., Burlando, P., Bou-Zeid, E., Chow, W.T.L., Coutts, A.M., Daly, E., Nice, K.A., Roth, M., Tapper, N.J., Velasco, E., Vivoni, E.R., Fatichi, S., 2020. An urban ecohydrological model to quantify the effect of vegetation on urban climate and hydrology (UT&C v1.0). Geosci. Model Dev. 13, 335–362. https://doi.org/10.5194/gmd-13-335-2020.
- Mirocha, J., Kirkil, G., Bou-Zeid, E., Chow, F.K., Kosović, B., 2013. Transition and equilibration of neutral atmospheric boundary layer flow in one-way nested large-Eddy simulations using the weather research and forecasting model. Mon. Weather Rev. 141, 918–940. https://doi.org/10.1175/MWR-D-11-00263.1.
- Nahian, M.R., Nazem, A., Nambiar, M.K., Byerlay, R., Mahmud, S., Seguin, A.M., Robe, F.R., Ravenhill, J., Aliabadi, A.A., 2020. Complex meteorology over a complex mining facility: assessment of topography, land use, and grid spacing modifications in WRF. J. Appl. Meteorol. Climatol. 59, 769–789. https://doi.org/10.1175/JAMC-D-19-0213.1.
- Park, S.B., Baik, J.J., Han, B.S., 2015. Large-eddy simulation of turbulent flow in a densely built-up urban area. Environ. Fluid Mech. 15, 235–250. https://doi.org/10.1007/s10652-013-9306-3.
- Ramamurthy, P., Bou-Zeid, E., 2014. Contribution of impervious surfaces to urban evaporation. Water Resour. Res. 50, 2889–2902. https://doi.org/10.1002/2013WR013909.
- Ramamurthy, P., Bou-Zeid, E., 2017. Heatwaves and urban heat islands: a comparative analysis of multiple cities. J. Geophys. Res. Atmos. 122, 168–178. https://doi.org/10.1002/2016JD025357.
- Ramamurthy, P., Bou-Zeid, E., Smith, J.A., Wang, Z.-H., Baeck, M.L., Saliendra, N.Z., Hom, J.L., Welty, C., 2014. Influence of subfacet heterogeneity and material properties on the urban surface energy budget. J. Appl. Meteorol. Climatol. 53, 2114–2129. https://doi.org/10.1175/JAMC-D-13-0286.1.
- Ren, G.Y., 2015. Urbanization as a major driver of urban climate change. Adv. Clim. Chang. Res. https://doi.org/10.1016/j.accre.2015.08.003.
- Richards, L.A., 1931. Capillary conduction of liquids through porous mediums. J. Appl. Phys. 1, 318-333. https://doi.org/10.1063/1.1745010.
- Ryu, Y.-H., Bou-Zeid, E., Wang, Z.-H., Smith, J.A., 2016a. Realistic representation of trees in an urban canopy model. Boundary-Layer Meteorol. 159, 193–220. https://doi.org/10.1007/s10546-015-0120-y.
- Ryu, Y.-H., Smith, J.A., Bou-Zeid, E., Baeck, M.L., 2016b. The influence of land surface heterogeneities on heavy convective rainfall in the Baltimore–Washington metropolitan area. Mon. Weather Rev. 144, 553–573. https://doi.org/10.1175/MWR-D-15-0192.1.
- Schaake, J.C., Koren, V.I., Duan, Q.Y., Mitchell, K., Chen, F., 1996. Simple water balance model for estimating runoff at different spatial and temporal scales. J. Geophys. Res. Atmos. 101, 7461–7475. https://doi.org/10.1029/95JD02892.
- Seck, A., Welty, C., Maxwell, R.M., 2015. Spin-up behavior and effects of initial conditions for an integrated hydrologic model. Water Resour. Res. 51, 2188–2210. https://doi.org/10.1002/2014WR016371.
- Senatore, A., Mendicino, G., Gochis, D.J., Yu, W., Yates, D.N., Kunstmann, H., 2015. Fully coupled atmosphere-hydrology simulations for the Central Mediterranean: impact of enhanced hydrological parameterization for short and long time scales. J. Adv. Model. Earth Syst. 7, 1693–1715. https://doi.org/10.1002/2015MS000510.
- Seto, K.C., Shepherd, J.M., 2009. Global urban land-use trends and climate impacts. Curr. Opin. Environ. Sustain. 1, 89–95. https://doi.org/10.1016/J. COSUST.2009.07.012.
- Shrestha, P., Sulis, M., Masbou, M., Kollet, S.J., Simmer, C., 2014. A scale-consistent terrestrial systems modeling platform based on COSMO, CLM, and ParFlow. Mon. Weather Rev. 142, 3466–3483. https://doi.org/10.1175/MWR-D-14-00029.1.
- Skamarock, W.C., Klemp, J.B., Dudhia, J., Gill, D.O., Barker, D.M., Duda, M.G., Huang, X.-Y., Wang, W., Powers, J.G., 2008. A description of the advanced research WRF version 3. NCAR Tech. Note. https://doi.org/10.5065/D68S4MVH.
- Spyrou, C., Varlas, G., Pappa, A., Mentzafou, A., Katsafados, P., Papadopoulos, A., Anagnostou, M.N., Kalogiros, J., 2020. Implementation of a nowcasting hydrometeorological system for studying flash flood events: the case of Mandra, Greece. Remote Sens. 12 https://doi.org/10.3390/RS12172784.
- Talbot, C., Bou-Zeid, E., Smith, J., 2012. Nested Mesoscale large-Eddy simulations with WRF: performance in real test cases. J. Hydrometeorol. 13, 1421–1441. https://doi.org/10.1175/JHM-D-11-048.1.
- Vahmani, P., Hogue, T.S., 2014. Incorporating an urban irrigation module into the Noah land surface model coupled with an urban canopy model. J. Hydrometeorol. 15, 1440–1456. https://doi.org/10.1175/JHM-D-13-0121.1.
- Varlas, G., Anagnostou, M.N., Spyrou, C., Papadopoulos, A., Kalogiros, J., Mentzafou, A., Michaelides, S., Baltas, E., Karymbalis, E., Katsafados, P., 2018. A multiplatform Hydrometeorological analysis of the flash flood event of 15 November 2017 in Attica, Greece. Remote Sens. 11, 45. https://doi.org/10.3390/rs11010045.
- Wagner, S., Fersch, B., Yuan, F., Yu, Z., Kunstmann, H., 2016. Fully coupled atmospheric-hydrological modeling at regional and long-term scales: development, application, and analysis of WRF-HMS. Water Resour. Res. 52, 3187–3211. https://doi.org/10.1002/2015WR018185.
- Wang, Z.-H., Bou-Zeid, E., Smith, J.A., 2011. A spatially-analytical scheme for surface temperatures and conductive heat fluxes in urban canopy models. Boundary-Layer Meteorol. 138, 171–193. https://doi.org/10.1007/s10546-010-9552-6.
- Wang, Z.-H., Bou-Zeid, E., Smith, J.A., 2013. A coupled energy transport and hydrological model for urban canopies evaluated using a wireless sensor network. Q. J. R. Meteorol. Soc. 139, 1643–1657. https://doi.org/10.1002/qj.2032.
- Wiersema, D.J., Lundquist, K.A., Chow, F.K., 2020. Mesoscale to microscale simulations over complex terrain with the immersed boundary method in the weather research and forecasting model. Mon. Weather Rev. 148, 577–595. https://doi.org/10.1175/mwr-d-19-0071.1.
- Wyngaard, J.C., 2004. Toward Numerical Modeling in the "Terra Incognita". J. Atmos. Sci. 61, 1816–1826. https://doi.org/10.1175/1520-0469(2004)061<1816: TNMITT>2.0.CO;2.